JACS
JOURNAL OF THE AMERICAN CHEMICAL SOCIETY
Article
pubs.acs.org/JACS

Evaluating the Contribution of Transition-State Destabilization to Changes in the Residence Time of Triazole-Based InhA Inhibitors

Lauren A. Spagnuolo,[†,#] Sandra Eltschkner,[§,#] Weixuan Yu,[†,#] Fereidoon Daryaee,[†] Shabnam Davoodi,[†] Susan E. Knudson,[‡] Eleanor K. H. Allen,[†] Jonathan Merino,[†] Annica Pschibul,[§] Ben Moree,[⊥] Neil Thivalapill,[∥] James J. Truglio,[∥] Joshua Salafsky,[⊥] Richard A. Slayden,[*,‡] Caroline Kisker,[*,§] and Peter J. Tonge[*,†]

[†]Institute of Chemical Biology and Drug Discovery, Department of Chemistry, Stony Brook University, Stony Brook, New York 11794-3400, United States

[§]Rudolf Virchow Center for Experimental Biomedicine, Institute for Structural Biology, University of Würzburg, 97080 Würzburg, Germany

[‡]Department of Microbiology, Immunology and Pathology, Colorado State University, Fort Collins, Colorado 80523-2025, United States

[⊥]Biodesy, Inc., 384 Oyster Point Boulevard, South San Francisco, California 94080, United States

[∥]Great Neck South High School, 341 Lakeville Road, Great Neck, New York 11020, United States

Supporting Information

ABSTRACT: A critical goal of lead compound selection and optimization is to maximize target engagement while minimizing off-target binding. Since target engagement is a function of both the thermodynamics and kinetics of drug−target interactions, it follows that the structures of both the ground states *and transition states* on the binding reaction coordinate are needed to rationally modulate the lifetime of the drug−target complex. Previously, we predicted the structure of the rate-limiting transition state that controlled the time-dependent inhibition of the enoyl-ACP reductase InhA. This led to the discovery of a triazole-containing diphenyl ether with an increased residence time on InhA due to transition-state destabilization rather than ground-state stabilization. In the present work, we evaluate the inhibition of InhA by 14 triazole-based diphenyl ethers and use a combination of enzyme kinetics and X-ray crystallography to generate a structure−kinetic relationship for time-dependent binding. We show that the triazole motif slows the rate of formation for the final drug−target complex by up to 3 orders of magnitude. In addition, we identify a novel inhibitor with a residence time on InhA of 220 min, which is 3.5-fold longer than that of the INH-NAD adduct formed by the tuberculosis drug, isoniazid. This study provides a clear example in which the lifetime of the drug−target complex is controlled by interactions in the transition state for inhibitor binding rather than the ground state of the enzyme−inhibitor complex, and demonstrates the important role that on-rates can play in drug−target residence time.

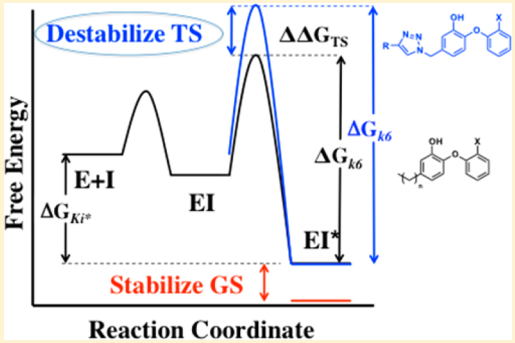

INTRODUCTION

Drug−target interactions often occur under conditions where the concentration of the drug or target is not constant, and thus both the thermodynamics and kinetics of drug binding are required to fully account for time-dependent changes in target occupancy in the human body.[1−4] However, often only equilibrium parameters such as IC_{50} values are used for selecting and optimizing drug candidates, neglecting the potential contribution that kinetic selectivity can make to the therapeutic index. This is important since the drug−target dissociation rate can be on the same time scale as clearance of the drug from the body, and thus even small changes in residence time can have a dramatic effect on designing dosing regimens that widen the therapeutic window.[5,6] Consequently, the structural and mechanistic factors that control the lifetime of a drug−target complex must be fully understood to deploy the power of drug−target kinetics in selecting and optimizing drug leads. While there is growing realization that drug−target binding kinetics can play a major role in improving the therapeutic window, several barriers exist, including the lack of extensive structure−kinetic relationships (SKRs) to guide the development of compounds with altered drug−target residence times, and insufficient knowledge of the molecular factors that control the lifetime of the drug−target complex.

Received: October 25, 2016
Published: February 2, 2017

DOI: 10.1021/jacs.6b11148
J. Am. Chem. Soc. 2017, 139, 3417−3429

InhA, the FabI enoyl-ACP reductase from *Mycobacterium tuberculosis*, is inhibited by the tuberculosis drug isoniazid through the formation of an INH-NAD adduct which is a slow-onset inhibitor of InhA.[7−9] Since resistance to isoniazid primarily arises from mutations in KatG,[10,11] the enzyme responsible for activating isoniazid, there has been a concerted effort to develop direct inhibitors of InhA that do not require activation by KatG.[12−21] In the course of our InhA−inhibitor discovery program, we have identified a series of compounds that inhibit the enzyme through a two-step slow-onset induced-fit mechanism in which the rapid formation of the initial enzyme−inhibitor (EI) complex is followed by a slow step leading to the final EI* complex (Scheme 1).[22]

Scheme 1. Two-Step Induced-Fit Inhibition Mechanism

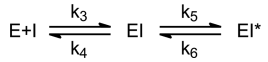

Previously, we used a combination of molecular dynamics (MD) simulations and X-ray crystallography to map the pathway between the EI and EI* states in InhA.[23] This study used the X-ray structure of InhA in complex with a rapid reversible inhibitor (**PT155**) to define the conformation of EI, and the structure of InhA bound to several slow-onset inhibitors to define the conformation of EI*. The MD simulations revealed that the transition state for interconversion of the EI and EI* states involved a steric clash between the side chains of residues in α-helix 6 and α-helix 7 which comprise the substrate-binding loop (SBL) in InhA.[23] We evaluated our model for slow-onset inhibition by introducing mutations that reduced the steric clash and decreased the lifetime of the corresponding drug−target complex. We then designed a triazole-based inhibitor, **PT163**, that re-introduced the steric clash through its bulky side chain, resulting in a longer residence time on the mutant InhA.[24] While **PT163** also had a longer residence time on wild-type InhA, the change in the off-rate (k_6 in Scheme 1) was not accompanied by an alteration in K_i^{*app}, the dissociation constant for the final EI* complex, suggesting a specific effect on the rate-limiting transition state on the binding reaction coordinate.[24]

Since triazoles are formed by reactions of alkynes with azides, click chemistry offers a strategy to interrogate the SKR for InhA inhibition while providing a platform for improving the drug-like properties of the diphenyl ether-based scaffold. We performed a full kinetic characterization of 15 triazole-based diphenyl ethers and 5 alkyl-based diphenyl ethers and compared the SKRs between the two sets of compounds to elucidate the role that on-rates play in modulating the stability of the enzyme−inhibitor complex. Progress curve analysis was used to determine values for K_i^{app}, the apparent dissociation constant for the initial EI complex ($K_i^{app} = k_4/k_3$), K_i^{*app}, the apparent dissociation constant for the final EI* complex, and k_6, the rate constant for conversion of EI* to EI. These parameters were then used to calculate k_5, the rate constant for conversion of EI to EI*, using $K_i^{*app} = K_i^{app}(k_6/(k_6+k_5))$, and the overall bimolecular rate constant $k_{on,overall}$ for formation of EI* from E +I using $k_{on,overall} = (k_5+k_6)/K_i^{app}$, based on the assumption that $k_6 \approx k_{off}$, the rate constant for formation of active enzyme from EI*.

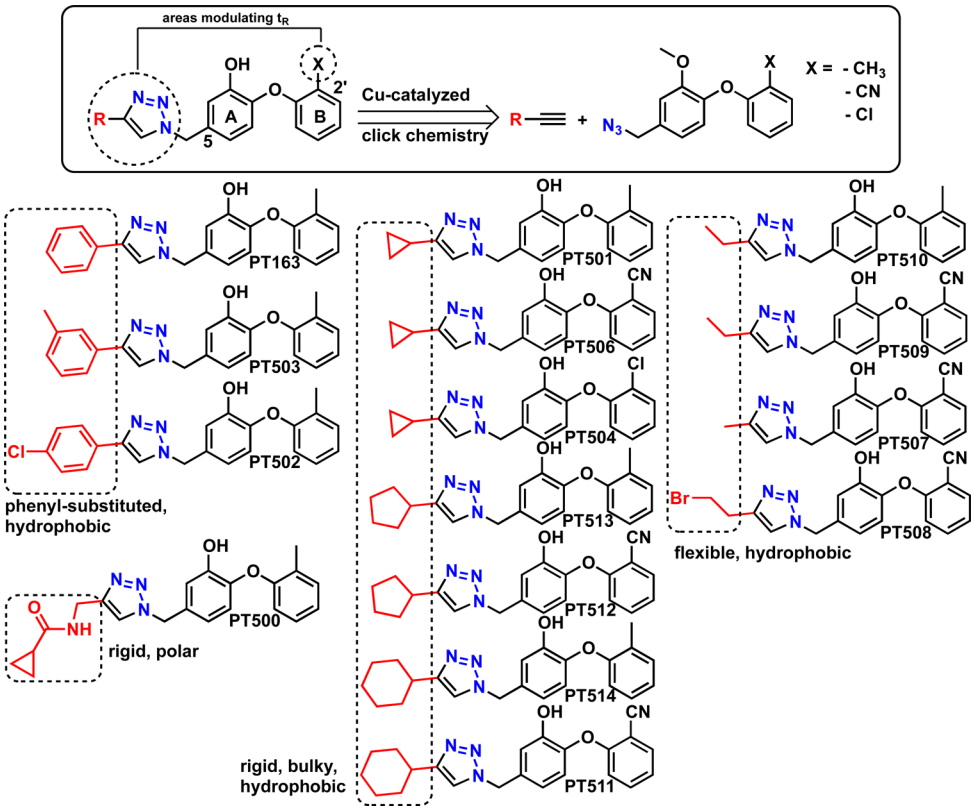

Figure 1. Triazole-based diphenyl ethers. Circled areas on the diphenyl ether scaffold highlight the positions that modulate residence time. The A-ring and B-ring of the diphenyl ether scaffold are indicated with the 5- and 2′-positions labeled. Categories of the different A-ring side chains are represented in the boxes.

DOI: 10.1021/jacs.6b11148
J. Am. Chem. Soc. 2017, 139, 3417−3429

Table 1. Chemical and Biological Data for the Diphenyl Ether Inhibitors[a]

Compound			MIC (μg/mL)	clogP[b] (clogD)	K_i^{app} (nM)	K_i^{*app} (nM)	k_5 (min^{-1})	$k_{on,\ overall}$ ($M^{-1}\ min^{-1}$)	k_6 (min^{-1})	t_R[c] (min); (t_R direct dissociation)
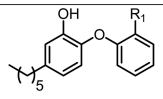										
	R_1									
PT70	CH_3		3.13	6.97 (5.99)	210 ± 34	29 ± 4	0.23	1.2×10^6	0.036 ± 0.010	30±7; (40±4)
PT113	F		1.56	6.41	220 ±6	27 ± 1	0.18	9.6×10^5	0.026 ± 0.004	38±5; (31±5)
PT91	Cl		1.56	6.95	52 ± 25	5.0 ± 2.0	0.12	2.5×10^6	0.013 ± 0.005	90±37; (148±13)
PT92	Br		3.13	7.1	120 ± 1	34 ± 1	0.28	3.3×10^6	0.11 ± 0.014	9.0±1; (42±7)
PT119	CN		2.5	5.90 (5.47)	10000 ± 2000	40 ± 1	5.0	5.0×10^5	0.020 ± 0.0040	50±0.4; (47±4)
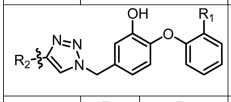										
	R_1	R_2								
PT500	CH_3		12.5	2.2	1800000	N/A[d]	N/A[d]	N/A[d]	RR[e]	N/A[d]
PT501	CH_3		0.78	3.6 (3.25)	17000 ± 3000	70 ± 14	1.2	7.4×10^4	0.005 ± 0.002	190±10; (206±15)
PT502	CH_3		6.25	5.8	1900 ± 500	77 ± 15	0.34	1.9×10^5	0.014 ± 0.011	55±8
PT503[a]	CH_3		6.25	5.5	6600 ± 300	100 ± 10	0.56	8.6×10^4	0.008 ± 0.001	110±2; (97±12)
PT504	Cl		0.156	3.62	16000 ± 10000	68 ± 9	1.1	6.9×10^4	0.0047 ± 0.0011	220±49; (625±78)
PT506	CN		0.313	3.98 (2.77)	99000 ± 16000	370 ± 10	1.4	1.4×10^4	0.0052 ± 0.0002	194 ± 3
PT507	CN		0.625	3.59	28000 ± 7000	1060 ± 200	0.28	1.0×10^4	0.0108 ± 0.0002	92±2
PT508	CN		0.625	3.55	7100 ± 1400	150 ± 30	0.50	7.1×10^4	0.0107 ± 0.002	93±18
PT509	CN		1.25	5.5	50000 ± 10000	1190 ± 200	0.91	1.9×10^4	0.0222 ± 0.0003	45±1
PT510	CH_3		0.625	5.5	110000 ± 20000	280 ± 60	10.5	9.5×10^4	0.0267 ± 0.0003	37±1
PT511	CN		0.625	4.5	6300 ± 1300	190 ± 37	0.27	4.5×10^4	0.0084 ± 0.0017	119±23
PT512	CN		0.625	4.2	83000 ± 17000	350 ± 70	2.23	2.7×10^4	0.0094 ± 0.0018	106±21
PT513	CH_3		1.56	4.7	45000 ± 12000	298± 41	3.99	8.9×10^4	0.0266 ± 0.0047	38±7
PT514	CH_3		6.25	4.9	200000 ± 40000	610 ± 122	3.46	1.7×10^4	0.0106 ± 0.002	94±18
PT163[a]	CH_3		ND[f]	3.95	81000 ± 23000	233 ± 39	3.20	3.9×10^4	0.0092 ± 0.002	113±28; (114±18)

[a]All kinetic assays were performed at 25 °C except for two compounds noted where assays were performed at 20 °C. Errors are standard errors from global data analysis. [b]clogP values were determined using ChemDraw and clogD values were calculated using ACDLabs Suite. [c]Values in parentheses are the residence times determined from the ^{32}P-NAD$^+$ direct dissociation method. [d]N/A, not applicable. [e]RR, rapid reversible. [f]ND, not determined.

To further dissect the contribution that the on-rate plays in modulating the residence time of inhibitors on InhA, we used a second harmonic generation (SHG) method to monitor the kinetics of drug−target complex formation for three com-

DOI: 10.1021/jacs.6b11148
J. Am. Chem. Soc. 2017, 139, 3417−3429

pounds that were representative of the range of binding kinetics observed in compounds populating the EI and EI* states. Taken together, these studies add fine detail to our understanding of the molecular drivers that control the lifetime of InhA−inhibitor complexes, laying the foundation for the rational design of compounds with increased residence time through both ground-state stabilization and transition-state destabilization.

RESULTS AND DISCUSSION

Generation of a Click Chemistry Library To Interrogate Structure−Kinetic Relationships. The triazole is a privileged pharmacophore, found in the scaffolds of a number of drug discovery programs in addition to structures of marketed antibacterial compounds.[25,26] The triazole group is normally introduced using click chemistry, and thus triazole-based compounds are often the product of analogue-forming efforts aimed at generating structure−activity relationship (SAR) data.[25,27] To generate robust SKR data, we used click chemistry to synthesize 14 novel analogues of the triazole-diphenyl ether **PT163** (Figure 1). The synthetic route and synthetic procedures/characterization data for all these compounds can be found in the Experimental Methods section and in the Supporting Information, respectively.

The inhibition of InhA by the diphenyl ethers was analyzed by a substrate-based assay and found to exhibit slow-onset inhibition characteristic of many previous enoyl-ACP reductase inhibitors.[18] Details of the global fitting analysis are described in the Experimental Methods section. Briefly, the progress curve data were globally fit to the equations which describe a two-step induced-fit mechanism (Scheme 1; see Experimental Methods section), providing the thermodynamic (K_i^{app} and K_i^{*app}) and kinetic (k_6) constants for enzyme inhibition (Table 1). The values for K_i^{app}, K_i^{*app}, and k_6 were then used to obtain the rate constant for conversion of EI to EI* (k_5) and the overall k_{on} for formation of EI* ($k_{on,overall}$). In a separate experiment, the value of k_{off} was also determined for selected inhibitors using a direct dissociation method for comparison with the values of k_6 obtained by global fitting of the progress curve data.[28] These studies revealed that the triazole-diphenyl ethers had overall association rate constants ($k_{on,overall}$) that were 1−3 orders of magnitude slower than the association rates of the alkyl-diphenyl ethers. In addition, whereas values for k_5, the rate constant for conversion of EI to EI*, varied by ∼100-fold across all compounds, K_i^{app}, the dissociation constant for the initial EI complex, varied by ∼4000-fold, indicating that variation in inhibitor structure had a more profound impact on the barrier leading to formation of EI than on the barrier between EI and EI*.

The triazole series can be separated into three groups based on the nature of the 2′-position B-ring substituent, which is a methyl (−CH_3), chloro (−Cl), or cyano (−CN) group (Figure 1). To form a basis for comparing the effects of modulating the structure of the triazole analogues on enzyme inhibition, kinetic data are also included in Table 1 for hexyl-diphenyl ethers with −CH_3 (**PT70**), −Cl (**PT91**), and −CN (**PT119**) substituents at the B-ring 2′-position as well as the fluoro (**PT113**) and bromo (**PT92**) analogues. Below we compare and contrast the impact of replacing the alkyl group with the triazole-based substituents and rationalize the structure−kinetics trends within the triazole-diphenyl ether series.

InhA as an Ideal Model System for Probing SKRs. The biologically active unit of InhA is a tetramer. Each monomer consists of a central β-sheet, on top of which the cofactor is bound and which is surrounded by three α-helices on each side. The substrate binding pocket is shielded by the SBL, comprised of α-helices 6 and 7 and the loop that connects these helices. The SBL has to open and close during the process of substrate binding in each catalytic cycle. Upon inhibitor binding, a similar behavior can be observed, and depending on the nature of the inhibitor, different states of SBL closure are achieved.

InhA undergoes an isomerization event from an open (EI) to a closed (EI*) state upon binding to slow-onset inhibitors. The relative populations of these two conformations are driven by the residence time and depend on the stability of the final complex in addition to the energy barrier at the transition state between the two states. Figure 2 compares the closed SBL

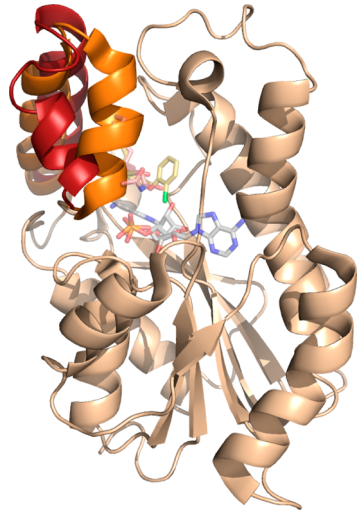

Figure 2. Conformations of the substrate binding loop (SBL). The SBL, which includes α-helix 6, the interconnecting loop, and α-helix 7, adopts a closed conformation in the structure of **PT91** bound to InhA (shown in orange, PDB: 4OYR) relative to that of the C16-NAC substrate analogue, which binds in a more open conformation (shown in red, PDB: 1BVR).

structure of InhA bound to **PT91**, representing EI*, with a more open SBL structure in which InhA is bound to the C16-NAC substrate analogue.[29] The conformation adopted in the closed state does not lie on the reaction coordinate for substrate turnover since residues from α-helix 6 occupy part of the active site where the substrate would normally bind.[23]

Crystal structures for 6 of the 14 novel triazole-based diphenyl ether inhibitors bound to InhA have been solved. Triazole-based diphenyl ethers also occupy the closed conformation, and before developing SKRs, it was important to understand similarities and differences between the alkyl- and triazole-based diphenyl ether compounds. The inhibitors differ in their substitution patterns, containing either a −CH_3, −Cl, or −CN group at their 2′-position, combined with either a 5-hexyl or a 5-triazole substituent to which a cyclic acyl chain is attached. The consequences of the 2′-substituents will be discussed below. 5-Hexyl-substituted diphenyl ethers are generally involved in multiple hydrophobic interactions within the substrate binding pocket. While the hexyl substituents form van der Waals contacts with F149, M199, I202 or V203, and L218, the protein−inhibitor interactions of the 5-triazole-substituted compounds are more extensive and more diverse in nature. The triazole ring is in close proximity to the aromatic

DOI: 10.1021/jacs.6b11148
J. Am. Chem. Soc. 2017, 139, 3417−3429

rings of Y158 and F149, and also to M199 and I202 or V203, depending on the conformational state of α-helix 6. In addition, in most cases a hydrogen bond is formed to either E219 or Q214. The size of the 5-cycloalkyl ring results in a large interaction surface within the substrate binding pocket of the protein, which is reflected by numerous hydrophobic interactions with the residues of α-helix 6 (I202 or V203) and α-helix 7 (I215, L217, L218) in the SBL.

To interrogate SKRs, it was important to compare the relative positions of α-helix 6 and α-helix 7 for a variety of InhA-bound conformations to address how open or how closed the SBL is in the presence of a given compound. Figure 3 summarizes the data for the structures of the triazole-diphenyl ethers and compares the conformational coordinates to other InhA-bound structures by presenting the location of all crystal structures on the same conformational plot, in which the SBL is defined by a shear and a step torsion angle (see details in Supporting Information).

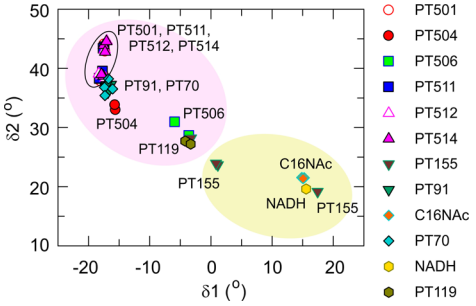

Figure 3. Conformational space populated by the SBL in different InhA-ligand structures. The torsion angles $\delta 1$ and $\delta 2$ are used to define the conformational space accessed by the SBL. Torsion angles have been taken from the X-ray structures of InhA in complex with the triazole- and alkyl-diphenyl ether inhibitors as well as NADH (PDB: 2AQ8) and C16-NAc (PDB: 1BVR). The lower right quadrant (light green) of the plot is populated by structures with a more open conformation of α-helix 6, whereas the upper left quadrant (light magenta) contains structures with a more closed conformation of α-helices 6 and 7. Rapid reversible inhibitors populate the EI state (open conformation), and slow-onset inhibitors populate the EI* state (closed conformation).

The SBL in complexes of InhA with the rapid-reversible inhibitor **PT155**, as well as with NADH or the C16-NAC substrate analogue, adopt a more open conformation, and these structures cluster toward the lower right quadrant of the conformational plot. In contrast, torsion angles for the SBL in complexes formed by the slow-binding compounds, including both the triazole- and alkyl-diphenyl ethers, cluster toward the upper left quadrant of the plot, since in these structures the SBL adopts a more closed conformation. In an attempt to quantify the degree of conformational change as well as the rates associated with the binding of inhibitors that occupy different positions on the conformational plot shown in Figure 3, the rapid-reversible inhibitor **PT155**, as well as a slow-binding alkyl- (**PT119**) and triazole-diphenyl ether (**PT504**), were selected for additional analysis using the conformationally sensitive SHG technique.[30−34] SHG is a nonlinear optical technique that is highly sensitive to the orientation of second-harmonic active molecules tethered to a surface. In the experiments performed here, we have labeled the protein with SHG-active dye and tethered the protein to a supported lipid bilayer surface on glass. The magnitude of the SHG signal intensity depends on the angle of the dye relative to the surface to which the protein is bound. Upon compound binding, changes in the angular orientation of the dye result in a change in the SHG intensity. The magnitude of the SHG signal change is dependent on the overall structural conformational change upon ligand binding, such that a larger conformational change is expected to produce a larger signal change for a given assay.[31,32] The SHG signal is proportional to the sixth power of the cosine of θ, the angle between the axis of the hyperpolarizability element of the dye and the surface normal, and thus the SHG technique has high sensitivity to angular change. In cases where all the dye molecules (and proteins) are aligned with a very narrow orientational distribution, i.e., all pointing in the same orientation, SHG can detect an angular change of ~1° at the label site, given the signal-to-noise ratio of the measurement.[32]

To enable SHG studies on InhA, an amine-reactive second-harmonic dye was covalently attached to the lysine residues of InhA using standard amide-bond coupling chemistry. The degree of labeling of InhA was determined spectrophotometrically to be 0.74 dye per monomer. Mass spectrometry was used to identify the position and extent of labeling and revealed that four lysines were modified: K57 (59%), K118 (21%), K132 (7%), and K181 (13%). As InhA is an obligate tetramer, the mass spectrometry results indicate the protein is heteroge-

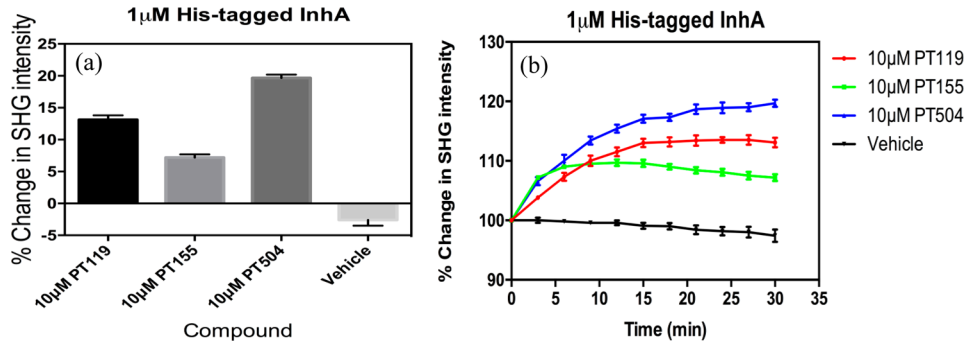

Figure 4. Binding-induced conformational changes in InhA detected by SHG. (a) Magnitude of the SHG signal change induced by ligand binding to InhA 30 min after compound addition. (b) The 30 min time course for approach to final conformational change upon inhibitor binding. SHG intensity has been normalized for the addition of each compound. The addition of each compound occurred shortly after the initial reading of the SHG intensity at $t = 0$. **PT119** corresponds to the red trace, **PT155** to the green trace, and **PT504** to the blue trace. The vehicle-only control trace is shown in black. For all experiments, $N = 4$ measurements were performed. Error bars = SEM.

DOI: 10.1021/jacs.6b11148
J. Am. Chem. Soc. 2017, 139, 3417−3429

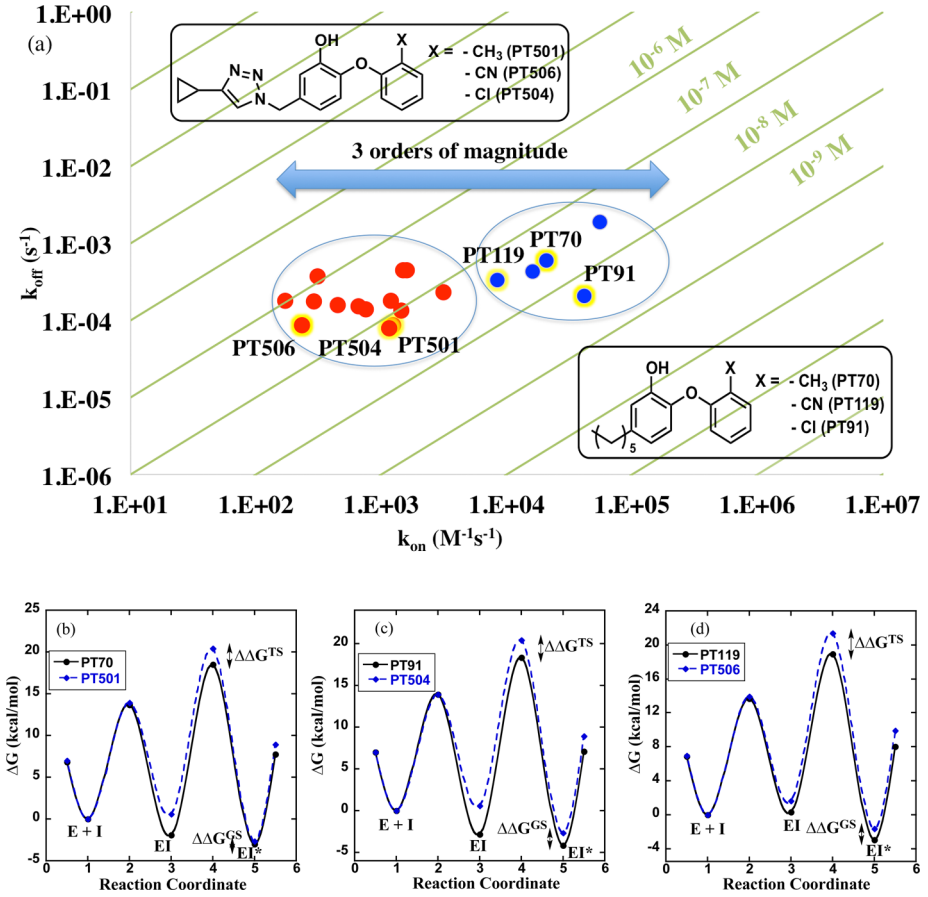

Figure 5. Kinetic map and free energy profiles for InhA inhibition. (a) 2-D kinetic map of k_{off} vs k_{on}, with diagonal lines showing K_i*. Free energy profiles comparing the inhibition of InhA by **PT70** and **PT501** (b), **PT91** and **PT504** (c), and **PT119** and **PT506** (d). This figure highlights the role of transition-state destabilization in increasing the residence time of the triazole-diphenyl ethers.

neously labeled at several residues throughout the core tetrameric structure.

After immobilizing the labeled protein on the Ni-NTA bilayer using an N-terminal His-tag, we next tested each compound for the ability to modulate the conformation of InhA by measuring the change in the SHG intensity upon compound addition. Each compound was added at 10 μM final concentration, and the change in SHG intensity was measured over a 30 min time course. As can be seen in Figure 4a, the addition of compound **PT155** to His-tagged InhA resulted in an increase of 7.2 ± 0.6% in the SHG intensity of the labeled, surface-tethered protein. The addition of compounds **PT119** and **PT504** also resulted in an increase in the SHG intensity of 13.1 ± 0.8% and 19.7 ± 0.6%, respectively. A control vehicle injection was also performed, and the change in SHG intensity over the time course was measured as −2.6 ± 1.0%. Comparison of the change in SHG intensity indicated that the response of each compound was significantly different than that of the vehicle control. In addition, the data indicate that the change in SHG intensity upon injection of each compound was significantly different compared to those for the other compounds in the series. The different signal change results suggest that **PT155**, **PT119**, and **PT504** all induce distinct conformations of InhA upon binding. While binding of **PT155** is accompanied by the smallest degree of change relative to the control, binding of **PT119** and **PT504** is accompanied by a larger degree of conformational change, which agrees with the structural data in Figure 3, where **PT155** occupies the most open conformation, followed by **PT119** and, last, **PT504**, which is the most closed of the three selected compounds. Therefore, the SHG measurements of the degree of conformational change of the protein in solution are consistent with the changes observed in the crystal structures.

In addition to the magnitude of the conformational change, the SHG data in Figure 4b indicate that the time course of conformational change is distinct for compound **PT155** compared to compounds **PT119** and **PT504**. The addition of **PT155** results in a step-like increase in the SHG intensity of InhA, consistent with the kinetic data, indicating the compound is a rapid-binding, reversible inhibitor. This result is in contrast to the time courses obtained for compounds **PT119** and **PT504**, which require a longer time to reach a plateau compared to **PT155**. This difference in the rate of conformational change shows that the kinetics of **PT119** and **PT504** binding are substantially different than for **PT155**. Finally, we simulated the experimental data obtained from the SHG assay using the kinetic and thermodynamic parameters obtained from progress curve analysis for **PT119** and **PT504** (Table 1), which involved estimating the levels of E, EI, and EI* using 10 μM inhibitor and 1 μM InhA. This approach was able to reproduce the SHG data (Figures S2−S4), indicating that the SHG technique provides an alternative method for the detection of slow-binding inhibitors.

Triazole-Based Diphenyl Ethers Modulate Residence Time by Transition-State Destabilization. Alterations in drug−target residence time occur through modulation in the

DOI: 10.1021/jacs.6b11148
J. Am. Chem. Soc. 2017, 139, 3417−3429

magnitude of the barrier between the ground and transition states on the binding reaction coordinate. This can occur by changes in the overall affinity of a drug for a target and/or by changes in the stability of the rate-limiting transition state(s). An increase in affinity will lead to an increase in residence time if stabilization of the drug−target complex ground state is not accompanied by changes to the transition state. However, there are examples where a change in residence time is not accompanied by a corresponding increase in potency.[35] In this case, changes in $k_{on,overall}$ and k_6 for a two-step inhibition mechanism can provide insight into explicit effects on the rate-limiting transition state for formation and breakdown of the final EI complex (EI* for a two-step mechanism). Indeed, in the limiting scenario where an increase in residence time occurs without a change in thermodynamic affinity, there must be a corresponding decrease in the on-rate for formation of the drug−target complex. Thus, as noted by Schoop and Dey,[36] a complete structure−kinetic analysis must include both the on- and off-rates for drug−target binding. In this regard, the contribution of $k_{on,overall}$ to changes in residence time and the overall affinity of the drug for the target can be assessed using a two-dimensional (2-D) kinetic map. In Figure 5a, the on- and off-rate data are shown for both the triazole- and alkyl-diphenyl ethers, where it can be seen that the two compound classes are clustered separately on the 2-D plot. In general, the triazole analogues have longer residence times than the alkyl-diphenyl ethers but bind either with similar potency or less tightly to the enzyme—thus, the residence times of the triazoles result from significantly slower on-rates (~100−1000-fold slower) than those of corresponding alkyl compounds, a result that can be clearly visualized on the kinetic map.

The kinetic map in Figure 5 indicates that the triazole substituents destabilize the rate-limiting transition state on the binding reaction coordinate relative to the corresponding alkyl analogues, which impacts both the rate of formation and the rate of breakdown of the EI* complex. In Figure 5b, the binding reaction coordinates for the B-ring methyl compounds **PT70** and **PT501** are plotted using 4 μM inhibitor as a reference value. **PT501** binds to InhA with ~2-fold lower affinity than **PT70** (K_i^{*app} = 70 and 29 nM, respectively) but with a residence time ~7-fold longer than that of **PT70**. These changes are accompanied by a 16-fold decrease in the on-rate for **PT501** (7.4×10^4 M^{-1} min^{-1} compared to 1.2×10^6 M^{-1} min^{-1} for **PT70**), and thus the triazole substituent has destabilized the transition state by ~1.7 kcal/mol relative to that of the corresponding alkyl-diphenyl ether. Comparisons of **PT91** and **PT504** (B-ring chloro), as well as **PT119** to **PT506** (B-ring cyano), shows similar trends (Figure 5).

Analogues with a B-Ring Cyano Group Have a Reduced Affinity to InhA, Which Is Accompanied by Slower On-Rates. In Figure 6 we show an expanded kinetic map for the triazole-diphenyl ethers. Except for the **PT511** (B-ring −CN)/**PT514** (B-ring $-CH_3$) pair, which have bulky cyclohexyl A-ring substituents (discussed later), replacement of a B-ring $-CH_3$ group with a −CN substituent generally results in a reduction in the on-rate. This is observed for analogues with cyclopropyl (**PT506** (−CN) and **PT501** ($-CH_3$)), ethyl (**PT509** (−CN) and **PT510** ($-CH_3$)), and cyclopentyl (**PT512** (−CN) and **PT513** ($-CH_3$)) substituents. This trend is also observed within the alkyl-diphenyl ether series, for example, comparison of **PT119** (−CN) and **PT70** ($-CH_3$). The slower on-rates of these pairs of compounds are coupled to comparable or weaker binding affinity, as shown in the kinetic

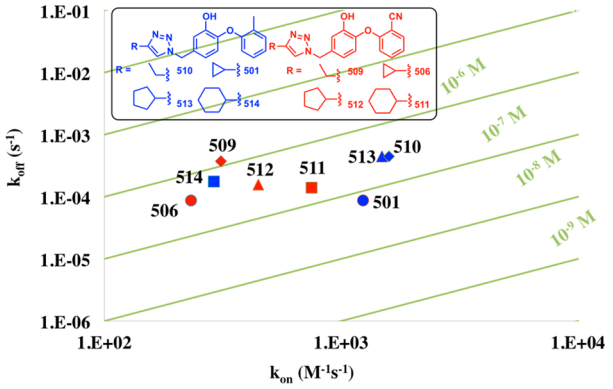

Figure 6. 2-D kinetic map for the triazole inhibitors. Analogues with 2′-CN substituents are shown in red and those with 2′-CH_3 substituents in blue. All 2′-CN analogues are shifted left relative to the 2′-CH_3 derivatives, except for the **PT511**/**PT514** pair. 2′-CN analogues have slower on-rates and weaker binding, causing little to no change in residence time compared to the 2′-CH_3 analogues.

map. This indicates modest to no change in residence time between the 2′-CN and 2′-CH_3 analogues with similar A-ring tails. Figure 6 shows that the on-rate for **PT506** relative to **PT501** is 5-fold slower and that this lateral shift is accompanied by no change in residence time.

Analysis of the structural data reveals that the 2′-CN group lacks the favorable hydrophobic interactions that the 2′-Cl and 2′-CH_3 analogues make with the enzyme (Figure 7). Specifically, in both triazole- and alkyl-diphenyl ether structures, the 2′-substituent is accommodated in a mostly hydrophobic environment formed by G96, A198 from α-helix 6, and the ribose pyrophosphate portion of the cofactor.

We speculate that the orientation of the 2′-substituents may partly be responsible for differences in time-dependent inhibition between analogues with 2′-CN substituents compared to those with 2′-Cl or 2′-CH_3 substituents. Upon binding to the enzyme, the 2′-CN group has to move past the carbonyl oxygen of G96 to form a hydrogen bond with the backbone NH group. Since the interaction with the partially negatively charged carbonyl oxygen is unfavorable, this could contribute to the energy barrier that has to be overcome upon binding, and it may take more time for the 2′-CN substituent to be properly positioned in the binding pocket and to reach its final, energetically lowest state. Thus, it is likely that the lack of stabilizing van der Waals contacts between A198 and G96 coupled with the electronic repulsion and only modest hydrogen-bonding to the backbone of G96 account for slower binding of the polar 2′-CN substituent in the hydrophobic pocket compared to the 2′-Cl and 2′-CH_3 analogues.

A comparison of the orientation of the 2′-substituents in different InhA-diphenyl ether complex structures reveals significant differences, particularly between the 2′-CN in contrast to the 2′-Cl and 2′-CH_3 groups. The most striking difference can be seen in comparing the distances between the 2′-substituents and the C_α of A198 (Figure 7). The 2′-Cl substituents of **PT91** and **PT504** and also the 2′-CH_3 groups of **PT501** and **PT514** tend to be oriented more toward A198, thereby forming close van der Waals contacts with the C_α of A198. Considering only subunits with fully defined SBLs, van der Waals distances ranging from 3.2 (**PT504**) to 3.5 Å (**PT91**) and from 3.2 to 3.5 Å within the InhA·NAD^+·**PT501** structures can be observed. In contrast, the 2′-CN groups are oriented farther away from A198 and located in closer proximity to G96,

DOI: 10.1021/jacs.6b11148
J. Am. Chem. Soc. 2017, 139, 3417−3429

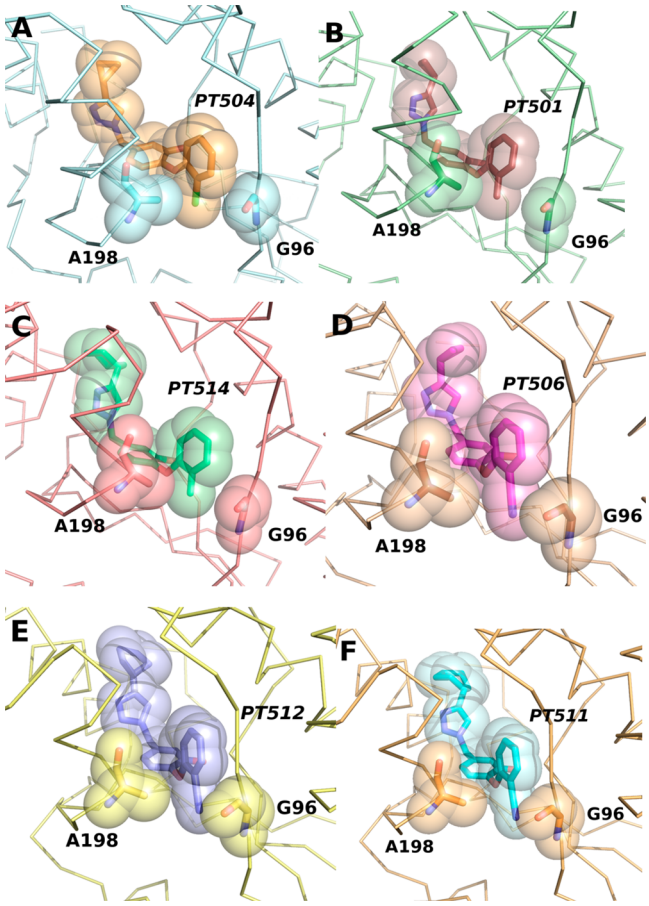

Figure 7. Interactions of the 2′-substituent with the enzyme. The 2′-substituents interact with G96 and A198 in the InhA substrate binding pocket: (A) **PT504**, (B) **PT501**, (C) **PT514**, (D) **PT506**, (E) **PT512**, and (F) **PT511**. The −Cl and $-CH_3$ groups of **PT501**, **PT504**, and **PT514** form van der Waals interactions with A198. The −CN group in **PT506**, **PT511**, and **PT512** lacks favorable contacts with A198 and could form a weak hydrogen bond with the backbone NH of G96, but that also could be accompanied by an unfavorable interaction with the backbone carbonyl of G96.

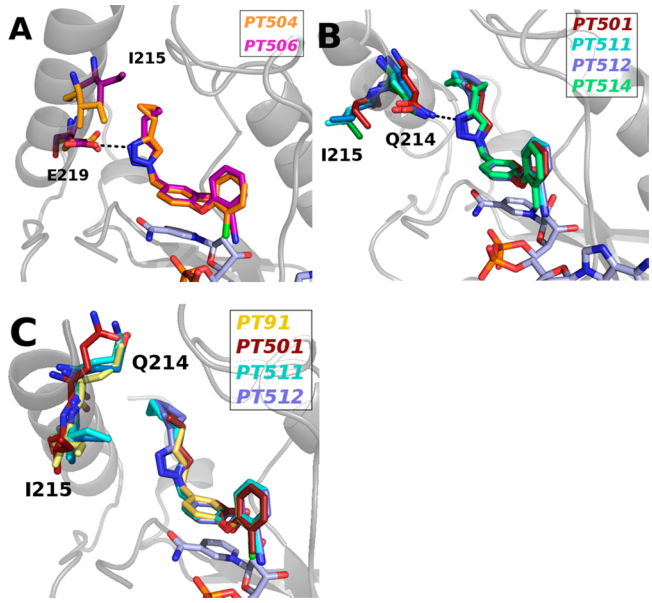

Figure 8. Interaction of α-helix 7 with the 5-substituent. (A) Hydrogen-bonding interaction of **PT504** (orange) and **PT506** (magenta) with E219 and the inward-rotated I215. (B) Hydrogen-bonding interaction of **PT501** (ruby), **PT511** (cyan), **PT512** (blue), and **PT514** (green) with Q214 and I215 pointing out of the hydrophobic pocket. (C) Absence of the hydrogen bond with Q214 or E219 and inward rotation of I215: **PT501** (ruby), **PT511** (cyan), and **PT512** (blue) compared to the **PT91** conformation (yellow).

although still not close enough to be in optimal hydrogen-bonding distance to the backbone NH of G96: this distance ranges from 3.1 Å in the InhA·NAD^+·**PT512** to 3.6 Å for **PT506**. In addition, an unfavorable interaction with the carbonyl group of G96 may also be present. Interestingly, because of the tilted arrangement of the 2′-CN group in the bound state, the carbon atom of this group approaches the C_α of A198, leading to a reduction in the distance to NH of G96, which may lead to an additional weak van der Waals contact with the C_α of A198 and thereby be beneficial for SBL stability. Our structural data therefore suggest that hydrophobic 2′-substituents, especially the smaller 2′-Cl group or 2′-CH_3 group, are preferable in this position since they permit a closer approach to A198, allowing the SBL to adopt a more closed, stable state. In contrast, the more polar 2′-CN substituent forms sub-optimal interactions with A198, while the potentially favorable hydrogen bond to the NH group of G96 is likely offset by unfavorable interactions with the G96 carbonyl group.

Structural Features Unique to PT514 Suggest a Steric Limit Is Reached in the Active Site. While the 2′-CH_3 analogues have faster on-rates and cluster to the right of the 2-D kinetic map compared with the 2′-CN analogues with the same A-rings, **PT514** appears to be an outlier (Figure 6). **PT514** has a 4-fold slower on-rate compared with either **PT504** or **PT501** (1.7×10^4 vs 7×10^4 M^{-1} min^{-1}). As shown in Figure 8, the triazole ring can hydrogen bond with either E219 or Q214. Below we discuss the positions of surrounding residues on both α-helix 6 and α-helix 7 in an attempt to elucidate the differences in the molecular interactions among the triazole-based inhibitors.

In the structures of **PT504** and **PT506**, the side chain of I215 is oriented toward the inhibitor, and an additional hydrogen bond is formed between the triazole moiety and E219 (Figure 8). This buried state of I215 seems to be entropically favored, as this hydrophobic residue is shielded from solvent. The inward rotation of I215 in combination with the hydrogen bond formed to E219 might have a positive synergistic effect on the residence times of these inhibitors and seems to represent the energetically most favorable SBL conformation among the InhA−inhibitor complexes discussed here. However, this phenomenon only seems to be possible for the inhibitors **PT504** and **PT506**, which possess a more flexible and less bulky cyclopropane substituent combined with either a 2′-Cl or 2′-CN group. The residual space in the substrate binding pocket upon binding **PT504** or **PT506** presumably creates a higher degree of rotational freedom for α-helix 7, allowing the side chain of I215 to be accommodated and the side chain of E219 to reach into the substrate binding pocket and form a hydrogen bond.

In contrast, the more bulky 2′-CH_3 substituent in **PT501** makes a simultaneous inward rotation of I215 and hydrogen-bond formation with E219 impossible. This leads to a change of the hydrogen-bond donor from E219 to Q214 for larger inhibitors, including **PT501** as well as **PT511**, **PT512**, and **PT514** (Figure 8). Close examination of each monomeric unit

DOI: 10.1021/jacs.6b11148
J. Am. Chem. Soc. 2017, 139, 3417−3429

in the crystal structures reveals that α-helix 7 in the InhA complexes formed with **PT501**, **PT511**, and **PT512** can also adopt a conformation similar to complexes formed by the alkyl-diphenyl ethers in which I215 is oriented into the substrate binding pocket but in which there is no hydrogen-bonding interaction with either E219 or Q214 (Figure 8C).

We propose that, to reach a conformational state where I215 is oriented toward the hydrophobic pocket, a rotation of α-helix 7 may have to take place, where Q214 is moved upward with respect to the substrate binding pocket (Figure 9). During this

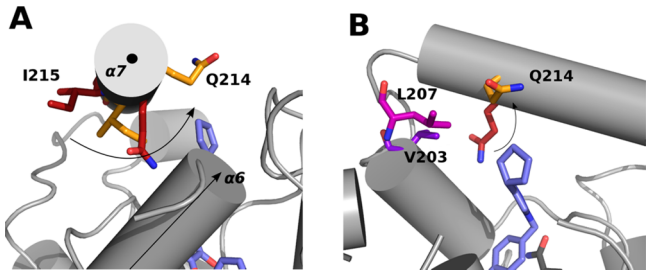

Figure 9. Proposed mechanism for α-helix 7 closure that prevents inward rotation of I215 upon binding of inhibitors that reach a "steric demand" limit. (A) View onto α-helix 7 (α7) along the rotation axis (depicted by a black dot). (B) View onto α7 perpendicular to the rotation axis. From the initial state (residues shown in red) Q214 has to pass the open space between the inhibitor's 5-cycloalkyl moiety and either V203 (purple, representing a more open conformation of α6) or L207 (magenta, representing a more closed conformation of α6) to reach the final state (residues shown in orange) where I215 is oriented into the hydrophobic pocket. The course of rotation is depicted by an arrow; an exemplary inhibitor is shown in blue.

rotation, Q214 would have to pass the open space between the 5-cycloalkyl substituent and either V203 or V207, depending on the extent to which α-helix 6 has closed. Consequently, the inward orientation of I215 is only possible within certain limits defined by the bulkiness of the 2′- and 5-substituents. In contrast to the **PT501**, **PT511**, and **PT512** InhA–inhibitor complexes, the structure of **PT514** bound to InhA does not display the "in"-state of I215 in any of the subunits, suggesting that the combination of a 2′-CH_3 group with a 5-cyclohexane ring exceeds the "steric limit" that would otherwise permit α-helix 7 to rotate.

Two monomer units (red and orange) of **PT512** bound to InhA are shown in Figure 9. The residues in red represent the "initial" hydrogen-bonded state whereby I215 is pointed out of the active site. The residues in orange represent the "I215-in" state. The proposed movement is shown by the arrow, marking the direction of rotation that α-helix 7 would have to make. This proposed motion is not possible for **PT514**, and for this reason, I215 is observed only in the "out" conformation.

We therefore hypothesize that a steric limit is reached in **PT514** with respect to space accommodation not only in the substrate binding pocket but also at the TS. Computational modeling suggests side chains on α-helices 6 and 7 slide past one another, and the cyclohexyl side chain of **PT514** likely pushes the boundaries of this clash, as indicated by a more than 4-fold decrease in the on-rate compared to **PT504** and **PT501**. We would expect a side chain that exceeds this limit to decrease residence time, and indeed **PT500**, which has a rigid carboxamide substituent, does not display slow-onset inhibition.

Since a similar trend is not observed within the 2′-CN B-ring series, it is hypothesized that the 2′-CN substituents, which have a smaller van der Waals radius than 2′-CH_3 compounds, do not approach a steric demand limit within the boundaries set by our click chemistry library. This is supported by our structural data upon comparison of single subunits harboring **PT511**, **PT512**, and **PT514** (Figure 8B,C). We speculate that further increasing the steric bulk of the A-ring tail will cause slower on-rates and eventual dissolution of residence time for the 2′-CN analogues.

Biological Properties of the Triazole-Based Diphenyl Ethers. In addition to its synthetic accessibility, the triazole group also has a number of favorable properties, including metabolic stability, the ability to function as a bioisostere for an amide group, and the ability to participate in $\pi-\pi$ stacking interactions.[25,37,38] Although the alkyl-diphenyl ethers have high affinity for InhA and antibacterial activity toward *M. tuberculosis*, these compounds display relatively high clogP values (6–7). Replacement of the hydrophobic alkyl substituent with a triazole moiety is expected to result in an improvement in clogP and an improved clogD, and some of our triazole-diphenyl ethers even have clogP values as low as 2.2 (Table 1). Further, compared to **PT119**, **PT70**, and **PT91**, the corresponding triazoles, namely, **PT506**, **PT501**, and **PT504**, respectively, have significantly improved clogD values, which have been described by Gerusz et al. to be important for decreasing the propensity of the scaffold to behave as a biocidal agent.[39] Interestingly, the improvement in clogP does not compromise antibacterial activity, and indeed **PT501** and **PT506** have minimum inhibitory concentration (MIC) values <1 μg/mL and clogP values that are ∼2–3 units lower than those of the corresponding alkyl-diphenyl ethers **PT70** and **PT119**, which have MIC values of 2–3 μg/mL.

■ CONCLUSION

A series of triazole-based diphenyl ethers have been synthesized using click chemistry in order to analyze the impact of introducing a triazole group into this class of compounds. In general, the triazole compounds have improved antibacterial activity and drug-like properties compared to the corresponding alkyl-diphenyl ethers. SKRs show that the triazole motif reduces the overall on-rate for association of the drug–target complex, effectively offering a novel strategy for modulating residence time in InhA. As the A-ring tail becomes larger and bulkier, structures show that key interactions become lost due to steric requirements. A 4-fold reduction in the on-rate for **PT514** compared to either **PT501** or **PT504** supports the presence of a steric clash at the transition state. This study demonstrates the need for understanding the contribution that both the on- and off-rates play in modulating residence time. It is therefore crucial to interrogate both SAR and SKR of a compound series to obtain a comprehensive analysis of the molecular factors driving drug–target engagement. Indeed, the on-rates of the triazole analogues fall into the "sweet spot" for k_{on}, 10^3-10^5 M^{-1} s^{-1}, described by Schoop et al.,[36] warranting further optimization of this compound series.

■ EXPERIMENTAL METHODS

InhA Purification. InhA was cloned and purified as described previously.[22,40] Briefly, the *InhA* gene from *M. tuberculosis* was cloned into either a pET15b or pET23b plasmid (Novagen) and transformed into *E. coli* BL21(DE3) pLysS cells. Following protein expression, the cells were lysed, and the InhA protein was purified via His-bind Ni^{2+}–

DOI: 10.1021/jacs.6b11148
J. Am. Chem. Soc. 2017, 139, 3417–3429

NTA affinity chromatography (Invitrogen) and size exclusion chromatography. The purified protein was >97% pure by SDS-PAGE and was stored at −80 °C in storage buffer consisting of either 20 or 30 mM PIPES, pH 6.8, containing 150 mM NaCl and 1 mM EDTA.

Progress Curve Analysis. Progress curve kinetics studies were performed on a Cary 100 UV−vis spectrophotometer (Varian) at 20 or 25 °C as described previously but with minor modifications.[28] Briefly, the reaction velocities were measured by monitoring the oxidation of NADH to NAD^+ at 340 nm. The enzyme reaction was initiated by adding 100 nM enzyme to C8-CoA (340 μM), NADH (250 μM), NAD^+ (200 μM), DMSO (2% v/v), inhibitor (0−20 μM), and 8% glycerol in 30 mM PIPES buffer, pH 6.8, containing 150 mM NaCl and 1 mM EDTA. The reaction was monitored until the progress curve became linear, suggesting the steady state had been reached. A high concentration of substrate and low concentration of enzyme were used to minimize substrate consumption and ensure that progress curves were linear in the absence of inhibitor. The progress curves were analyzed using the Morrison−Walsh integrated rate equation:

$$A_t = A_0 - v_s t - (v_i - v_s)\left(\frac{1 - e^{-k_{obs}t}}{k_{obs}}\right) \quad (1)$$

where A_t and A_0 are the absorbance values at time t and $t = 0$, v_i and v_s are the initial and steady-state velocity, respectively, and k_{obs} is the pseudo-first-order rate constant for the approach to the steady state. Equation 2 was then used to calculate k_6, which corresponds to the dissociation rate constant of the inhibitor from the enzyme:

$$k_6 = k_{obs}\left(\frac{v_s}{v_i}\right) \quad (2)$$

K_i^{app}, which corresponds to the apparent value of the K_i for the initial encounter complex, was determined by plotting the fractional initial velocities as a function of inhibitor concentration and fitting to the isotherm eq 3,

$$\frac{v_i}{v_0} = \frac{1}{1 + \frac{[I]}{K_i^{app}}} \quad (3)$$

where v_o is the control velocity from the uninhibited progress curve. K_i^{*app}, which represents the dissociation constant of the final EI* complex, was obtained by plotting the fractional steady-state velocities as a function of inhibitor concentration and fitting to the isotherm eq 4:

$$\frac{v_s}{v_0} = \frac{1}{1 + \frac{[I]}{K_i^{*app}}} \quad (4)$$

Data Analysis by Global Fitting. Progress curve measurements were performed in triplicate, and the data were fit to eq 1 using KaleidaGraph to provide estimates for v_0, v_i, v_s, and k_{obs}, from which values for K_i^{app} and K_i^{*app} together with their standard errors were calculated using eqs 3 and 4. The values for K_i^{app} and K_i^{*app} were constrained within the limits set by the standard error and provided input values for global fitting of all data sets to eqs 1−4, which in turn resulted in the optimum values for K_i^{app}, K_i^{*app}, and k_6 together with their standard errors. Values for k_5 and $k_{on,overall}$ were subsequently determined using eqs 5−8, where it is assumed that $k_6 \ll k_4$, k_5.[41]

$$k_6 \approx k_{off} = K_i^* k_{on,overall} \quad (5)$$

$$K_i^{*app} = K_i^{app}\left(\frac{k_6}{k_6 + k_5}\right) \quad (6)$$

$$k_6 = K_i^{app}\left(\frac{k_6}{k_6 + k_5}\right)k_{on,overall} \quad (7)$$

$$k_{on,overall} = \frac{k_6 + k_5}{K_i^{app}} \quad (8)$$

To validate the global fitting method, the value for k_6 was compared to the k_{off} value obtained using the ^{32}P-NAD^+ direct dissociation method described below. In all cases there was good agreement between k_6 and k_{off}, except for **PT92** and **PT504**, where k_{off} was 5- and 3-fold slower, respectively, than the value of k_6 (Table 1). In addition, for **PT92**, $k_6 \approx k_5$. Assuming that the dissociation rate obtained by the ^{32}P-NAD^+ direct dissociation method gives the true k_{off}, this value can be used to calculate $k_{on,overall}$ using eq 5, without making the assumptions that $k_6 \approx k_{off}$ or that $k_6 \ll k_4$, k_5. This approach gave values for $k_{on,overall}$ that were 4.7- and 2.9-fold slower than the values in Table 1. This does not change the conclusions drawn in the manuscript. Note that **PT70**, **PT91**, **PT92**, **PT113**, **PT119**, and **PT163** were re-analyzed using the global fitting analysis, and the values in Table 1 are similar to what has previously been reported.[15,23,24]

[^{32}P]-NAD^+ Direct Dissociation Kinetics. The direct dissociation kinetic experiments were performed as described.[28] In general, 500 μL of a solution containing 15 μM InhA, 20 μM NAD^+, [^{32}P]-NAD^+, and 200 μM inhibitor in 30 mM PIPES buffer, pH 6.8, containing 150 mM NaCl and 1 mM EDTA, was loaded onto a spin column followed by a 2 min centrifugation at 2500 rpm. The purified ternary complex solution was rapidly diluted into 60 mL of the reaction buffer to initiate ligand dissociation. Subsequently, 600 μL aliquots of the diluted mixture were collected at different time points, immediately loaded onto an ultrafiltration concentrator (Sartorius, 10 kDa), and centrifuged at 13 400 rpm for 90 s. The amount of ^{32}P in the flow-through was then quantified by scintillation counting (LS5801). Data were fit to eq 9, where $C(t)$ and $C(0)$ are the radioactive counts at time t and time 0, respectively, C_{max} is the maximum radioactive counts, and k_6 is the inhibitor dissociation rate constant:

$$C_t = C_0 + C_{max}(1 - e^{-k_6 t}) \quad (9)$$

Binding Kinetics Using SHG. *Protein Labeling.* InhA was labeled with the second-harmonic active amine reactive dye SHG1-SE (Biodesy, South San Francisco, CA). The labeling reaction was performed according to manufacturer's instructions. Briefly, InhA was exchanged into cold 100 mM $NaPO_4$, pH 7.5, and 150 mM NaCl prior to labeling, using a 7K MWCO Zeba desalting column (Thermo-Fisher). The protein was then diluted into cold labeling buffer to a final concentration of 30 μM protein, and a 2-fold molar excess of dye was added to the protein solution. The conjugation reaction was allowed to proceed for 10 min on ice, followed by centrifugation for 20 min at 16800*g*. The supernatant was then passed through a Zeba desalting column to remove free dye from the reaction and to exchange the protein into storage buffer (30 mM PIPES, pH 6.8, 150 mM NaCl, 8% glycerol). A Nano-Drop 2000 UV−vis spectrophotometer (Thermo-Fisher) was used to determine the degree of labeling as 0.74, using the known extinction coefficients of the dye and the protein at the absorbance maxima of 410 and 280 nm, respectively.

Mass Spectrometry Analysis. LC-MS/MS was performed by Martin Protean, LLC (Princeton, NJ), for a fee for service.

Sample and Compound Preparation. Bilayer formation and protein deposition were performed as previously described,[31] except with the following changes. A custom 384-well microtiter plate for high-throughput experiments was used for the formation of lipid bilayers and protein deposition (Biodesy Delta Read Plates). A Bravo automated liquid-handling platform (Agilent) with custom protocols was used for bilayer deposition, buffer washes, and protein deposition during sample preparation.

For InhA experiments, the assay buffer was 30 mM PIPES, pH 6.8, 150 mM NaCl, 8% glycerol, and 200 μM NAD^+. InhA protein was deposited at a final concentration of 1 μM in each well and allowed to incubate on the Ni-NTA surface for 1 h at room temperature. After incubation, unbound protein was removed by washing with assay buffer plus 1% DMSO. Plates were then allowed to equilibrate for 30 min at room temperature before beginning compound injections.

DOI: 10.1021/jacs.6b11148
J. Am. Chem. Soc. 2017, 139, 3417−3429

Scheme 2. Synthetic Route, Yields, and Compound Names for All Intermediates

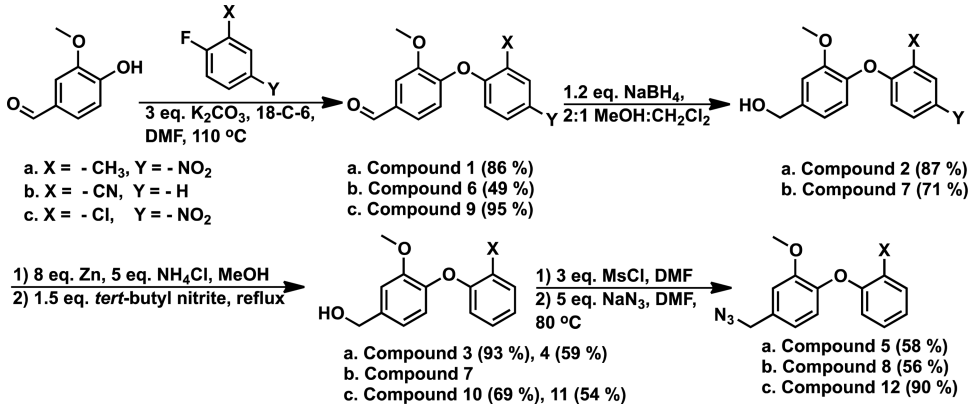

Compounds were prepared as 10 mM stocks in DMSO and then diluted into assay buffer to produce a final concentration of 10 μM (1% DMSO final) upon injection into the well. Experiments were performed in kinetic mode by monitoring the SHG signal in real time after compound injection. The signal was recorded over the course of 30 min with a 3-min interval time between reads.

SHG Instrumentation and Experiments. Experiments were performed on a Biodesy Delta System. The Biodesy Delta system is a 384-well microplate-based instrument, combining optical detection of the SHG signal with automated liquid handling to enable detection of conformational changes in real time, synchronized with ligand injection. Delta's optical subsystem comprises a femtosecond titanium sapphire (Ti:S) laser as the source of the fundamental beam at 800 nm. The fundamental beam is directed to an arrangement of prisms integrated with the custom, glass-bottomed Biodesy Delta Read Plates, where it undergoes total internal reflection (TIR) to generate the evanescent optical field at the glass–lipid bilayer interface. This field interacts with the SHG-active probe attached to the bilayer-tethered protein, generating the second-harmonic (SH) light at 400 nm, which emerges from the interface in a collimated beam nearly collinear with the fundamental beam. The fundamental light is filtered out, leaving only the SH light, which is detected by a photomultiplier tube and processed with custom electronics. The SHG signal is the intensity of the SH light (photons/s). The liquid-handling subsystem is designed to enable high-throughput, automated measurements using a standard 384-well microplate format. Ligand injection into the read plate is accomplished with an 8-channel MEMS-based electronic pipetting system, enabling high speed and accuracy. The system is controlled by a web-based user interface, enabling the user to visually design complex experiments utilizing multiple ligand plates. The software displays results in real time, numerically or graphically, and allows data to be exported for further analysis.

SHG Quantification. To plot the percent change in SHG intensity ($\%\Delta_{SH}$) over time, the second-harmonic baseline intensity measured just prior to injection (I_{t_0}) was subtracted from the second-harmonic intensity at each time interval t_n (I_{t_n}) and then divided by the initial SH intensity (I_{t_0}) according to eq 10:

$$\%\Delta_{SH} = (I_{t_n} - I_{t_0})/I_{t_0} \quad (10)$$

In addition, all experiments included a control buffer injection that was used to determine the threshold for SHG intensity change and was calculated in a similar manner. All values in the paper are reported as the mean ± SE of the percent change for each independent experiment. The SHG signal intensity, I (photons/s), is described by eq 11, where θ is the angle between the axis of the dye molecule and the surface normal and C is a constant:

$$I = C\langle \cos^6 \theta \rangle \quad (11)$$

The $\langle\ \rangle$ symbols denote an orientational average over all the molecules in the laser beam focus.

Data Analysis. The normalized SHG intensity values, calculated as indicated above, were imported into GraphPad Prism, and a one-way ANOVA with multiple comparisons was performed to determine the significance of the change in SHG intensity of each sample in the data set. Each sample was determined to be significantly different than the vehicle-only control ($p < 0.0001$) and relative to each compound ($p < 0.001$).

Substrate Synthesis. *trans*-2-Octenoyl coenzyme A (C8-CoA) was synthesized using the mixed anhydride method as described previously.[28] Briefly, 2 mmol of *trans*-2-octenoic acid was dissolved in 3 mL of dry tetrahydrofuran with 6 mmol of triethylamine under nitrogen. Following the addition of 6 mmol of ethyl chloroformate, the reaction was stirred at room temperature for 3 h under nitrogen. Subsequently, the reaction solution was centrifuged at 5000 rpm for 15 min to remove the precipitate, and the anhydride was added dropwise into a solution of CoA containing 50 mM Na_2CO_3, pH 8.0, and tetrahydrofuran (1:1) while being stirred at room temperature for 2 h. Acetic acid was added to prevent decomposition of the thioester, and excess organic solvent was removed by rotary evaporation. The crude mixture was centrifuged, and the bottom aqueous layer was purified using a CombiFlash 4.3 g C18 column. Chromatography was performed with 20 mM ammonium acetate as buffer A and 100% acetonitrile as buffer B over 60 min at a flow rate of 18 mL/min. Elution was monitored at 260 nm, and C8-CoA eluted at 20 column volumes over a linear gradient from buffer A to buffer B. The fractions containing substrate were pooled, and the acetonitrile was removed under reduced pressure, leaving the aqueous portion to be lyophilized. To remove all ammonium acetate, the substrate was redissolved in distilled H_2O and lyophilized two more times. Finally, the substrate was characterized by electrospray ionization mass spectrometry.

Compound Synthesis. The synthetic route, yields, and compound names for all intermediates are summarized in Scheme 2. The final two synthetic steps are the click reaction, followed by demethylation to afford the final phenol-containing compounds; see Supporting Information for details.

Techniques. NMR spectra (^{1}H and ^{13}C) were recorded on a Bruker-400 or Bruker-500 spectrometer in the indicated solvent at 25 °C. Chemical shifts are reported in δ, ppm. Flash chromatography was performed using CombiFlash R_f equipped with ResiSep R_f SiO_2 cartridges. All reactions were performed under N_2. Synthesis and characterization of the **PT500** series as well as all intermediates are described in the Supporting Information. **PT70**, **PT91**, **PT92**, **PT113**, **PT119**, and **PT163** were synthesized as described elsewhere.[15,22]

Crystallization and Structure Determination of InhA Ternary Complexes with PT501, PT504, PT506, PT511, PT512, and PT514. After 2 h of incubation on ice and centrifugation for 20 min at 16000 *g* and 4 °C the **PT501**-, **PT504**-, **PT506**-, **PT511**-, **PT512**-, and **PT514**-NAD^+-InhA complexes were crystallized by the hanging-drop vapor diffusion method at 20 °C. Crystals of the [InhA·NAD^+·**PT504**] and [InhA·NAD^+·**PT512**] complexes were obtained in 1.6 M sodium acetate, pH 7.0, with a 5-fold molar excess of cofactor and 50-fold molar excess of inhibitor over InhA at a protein concentration of 0.33

DOI: 10.1021/jacs.6b11148
J. Am. Chem. Soc. 2017, 139, 3417–3429

mM. The [InhA·NAD$^+$·**PT506**] complex crystallized under similar conditions at a higher sodium acetate concentration (2.4 M) but required only a 20-fold molar excess of **PT506**. Crystals of the InhA-**PT501** and -**PT514** complexes grew in conditions containing 2.5 or 3 M sodium chloride and 100 mM Tris-HCl, pH 8.0 or 9.0, at a 10- or 5-fold molar excess of cofactor, respectively, and 50-fold molar excess of inhibitor, utilizing InhA at a concentration of 0.33 mM. The complex of [InhA·NAD$^+$·**PT511**] did not provide crystals of sufficient quality using a simple crystallization setup. Hence, crystals from the InhA-PT501 crystallization setup (2.5 M sodium chloride and 100 mM Tris-HCl, pH 8.0) were diluted 1:100 in a buffer containing 20 mM PIPES, pH 6.8, 150 mM NaCl, and 1 mM EDTA and sonicated for 10 min. Next, 0.2 μL of the seeding solution was added to the protein drop containing InhA, NAD$^+$, and **PT511**. Crystals grew in 2.6 M sodium acetate, pH 7.0, with a 10-fold molar excess of cofactor and 20-fold molar excess of **PT511** over InhA (0.33 mM). Prior to data collection, the crystals were transferred to a cryoprotectant solution containing the mother liquor plus 26−35% ethylene glycol. Data sets were collected at beamline 14.1 at the BESSY II synchrotron or beamline P13 at the EMBL (only the [InhA·NAD$^+$·**PT511**] data set) using a Pilatus 6M detector. Data sets were processed with either Mosflm 7.0.9 (**PT504**, **PT512**) or XDS (**PT501**, **PT506**, **PT511**, **PT512**), and the structures were solved by molecular replacement utilizing the [InhA·NAD$^+$·**PT70**] complex structure (PDB: 2X23) as search model. Structure refinement was performed using the CCP4 suite with Refmac version 5.8.0073 for **PT506**, and Refmac 5.8.0155 for **PT501**, **PT504**, **PT511**, **PT512**, and **PT514** (Table S1).

MIC Determination. MIC values for the compounds were determined using a modified 96-well microplate Alamar Blue assay (MABA).[42] Briefly, *M. tuberculosis* was grown to early mid-log phase in Middlebrook 7H9 media supplemented with 10% OADC and 0.05% Tween 80. Compounds were two-fold serially diluted in triplicate in 96-well round-bottom microtiter plates. Media and growth controls were included. Bacteria were diluted to OD_{600nm} = 0.005 and added to the wells, and the plates were incubated at 37 °C for 6 days. Alamar blue was added, and the plates were incubated for an additional 24 h. The MIC was the drug concentration that inhibited visual growth and the reduction of Alamar blue in all replicates.

■ ASSOCIATED CONTENT

Supporting Information

The Supporting Information is available free of charge on the ACS Publications website at DOI: 10.1021/jacs.6b11148.

Data collection and refinement statistics for the InhA:inhibitor structures, definition of the torsion angles used in constructing Figure 3, SHG data for three compounds, details of the synthesis and characterization of the PT500 series, and NMR spectra for all final compounds (PDF)

■ AUTHOR INFORMATION

Corresponding Authors

*richard.slayden@colostate.edu
*caroline.kisker@virchow.uni-wuerzburg.de
*peter.tonge@stonybrook.edu

ORCID

Peter J. Tonge: 0000-0003-1606-3471

Author Contributions

#L.A.S., S.E., and W.Y. contributed equally to this work.

Notes

The authors declare no competing financial interest.

■ ACKNOWLEDGMENTS

This work was supported in part by the National Institutes of Health (grant GM102864 to P.J.T.) and by the Deutsche Forschungsgemeinschaft (grants SFB630 and Forschungszentrum FZ82 to C.K.). The authors thank Benjamin Merget (BioMed X, Heidelberg) and Christoph A. Sotriffer (University of Würzburg) for valuable discussions.

■ REFERENCES

(1) Copeland, R. A. *Nat. Rev. Drug Discovery* **2016**, *15*, 87−95.
(2) Copeland, R. A.; Pompliano, D. L.; Meek, T. D. *Nat. Rev. Drug Discovery* **2006**, *5*, 730−9.
(3) Lu, H.; Tonge, P. J. *Curr. Opin. Chem. Biol.* **2010**, *14*, 467−74.
(4) Walkup, G. K.; You, Z.; Ross, P. L.; Allen, E. K.; Daryaee, F.; Hale, M. R.; O'Donnell, J.; Ehmann, D. E.; Schuck, V. J.; Buurman, E. T.; Choy, A. L.; Hajec, L.; Murphy-Benenato, K.; Marone, V.; Patey, S. A.; Grosser, L. A.; Johnstone, M.; Walker, S. G.; Tonge, P. J.; Fisher, S. L. *Nat. Chem. Biol.* **2015**, *11*, 416−23.
(5) Cusack, K. P.; Wang, Y.; Hoemann, M. Z.; Marjanovic, J.; Heym, R. G.; Vasudevan, A. *Bioorg. Med. Chem. Lett.* **2015**, *25*, 2019−27.
(6) Zhang, R. *Nat. Chem. Biol.* **2015**, *11*, 382−3.
(7) Dessen, A.; Quemard, A.; Blanchard, J. S.; Jacobs, W. R., Jr.; Sacchettini, J. C. *Science* **1995**, *267*, 1638−41.
(8) Banerjee, A.; Dubnau, E.; Quemard, A.; Balasubramanian, V.; Um, K. S.; Wilson, T.; Collins, D.; de Lisle, G.; Jacobs, W. R., Jr. *Science* **1994**, *263*, 227−30.
(9) Rawat, R.; Whitty, A.; Tonge, P. J. *Proc. Natl. Acad. Sci. U. S. A.* **2003**, *100*, 13881−6.
(10) Lei, B.; Wei, C. J.; Tu, S. C. *J. Biol. Chem.* **2000**, *275*, 2520−6.
(11) Timmins, G. S.; Deretic, V. *Mol. Microbiol.* **2006**, *62*, 1220−7.
(12) Sink, R.; Sosic, I.; Zivec, M.; Fernandez-Menendez, R.; Turk, S.; Pajk, S.; Alvarez-Gomez, D.; Lopez-Roman, E. M.; Gonzales-Cortez, C.; Rullas-Triconado, J.; Angulo-Barturen, I.; Barros, D.; Ballell-Pages, L.; Young, R. J.; Encinas, L.; Gobec, S. *J. Med. Chem.* **2015**, *58*, 613−24.
(13) Manjunatha, U. H.; Rao, S. P.; Kondreddi, R. R.; Noble, C. G.; Camacho, L. R.; Tan, B. H.; Ng, S. H.; Ng, P. S.; Ma, N. L.; Lakshminarayana, S. B.; Herve, M.; Barnes, S. W.; Yu, W.; Kuhen, K.; Blasco, F.; Beer, D.; Walker, J. R.; Tonge, P. J.; Glynne, R.; Smith, P. W.; Diagana, T. T. *Sci. Transl. Med.* **2015**, *7*, 269ra3.
(14) Stec, J.; Vilcheze, C.; Lun, S.; Perryman, A. L.; Wang, X.; Freundlich, J. S.; Bishai, W.; Jacobs, W. R., Jr.; Kozikowski, A. P. *ChemMedChem* **2014**, *9*, 2528−37.
(15) Pan, P.; Knudson, S. E.; Bommineni, G. R.; Li, H. J.; Lai, C. T.; Liu, N.; Garcia-Diaz, M.; Simmerling, C.; Patil, S. S.; Slayden, R. A.; Tonge, P. J. *ChemMedChem* **2014**, *9*, 776−91.
(16) Hartkoorn, R. C.; Pojer, F.; Read, J. A.; Gingell, H.; Neres, J.; Horlacher, O. P.; Altmann, K. H.; Cole, S. T. *Nat. Chem. Biol.* **2014**, *10*, 96−8.
(17) Encinas, L.; O'Keefe, H.; Neu, M.; Remuinan, M. J.; Patel, A. M.; Guardia, A.; Davie, C. P.; Perez-Macias, N.; Yang, H.; Convery, M. A.; Messer, J. A.; Perez-Herran, E.; Centrella, P. A.; Alvarez-Gomez, D.; Clark, M. A.; Huss, S.; O'Donovan, G. K.; Ortega-Muro, F.; McDowell, W.; Castaneda, P.; Arico-Muendel, C. C.; Pajk, S.; Rullas, J.; Angulo-Barturen, I.; Alvarez-Ruiz, E.; Mendoza-Losana, A.; Ballell Pages, L.; Castro-Pichel, J.; Evindar, G. *J. Med. Chem.* **2014**, *57*, 1276−88.
(18) Pan, P.; Tonge, P. J. *Curr. Top. Med. Chem.* **2012**, *12*, 672−93.
(19) Vilcheze, C.; Baughn, A. D.; Tufariello, J.; Leung, L. W.; Kuo, M.; Basler, C. F.; Alland, D.; Sacchettini, J. C.; Freundlich, J. S.; Jacobs, W. R., Jr. *Antimicrob. Agents Chemother.* **2011**, *55*, 3889−98.
(20) Freundlich, J. S.; Wang, F.; Vilcheze, C.; Gulten, G.; Langley, R.; Schiehser, G. A.; Jacobus, D. P.; Jacobs, W. R., Jr.; Sacchettini, J. C. *ChemMedChem* **2009**, *4*, 241−8.
(21) Sullivan, T. J.; Truglio, J. J.; Boyne, M. E.; Novichenok, P.; Zhang, X.; Stratton, C. F.; Li, H. J.; Kaur, T.; Amin, A.; Johnson, F.; Slayden, R. A.; Kisker, C.; Tonge, P. J. *ACS Chem. Biol.* **2006**, *1*, 43−53.
(22) Luckner, S. R.; Liu, N.; am Ende, C. W.; Tonge, P. J.; Kisker, C. *J. Biol. Chem.* **2010**, *285*, 14330−7.

DOI: 10.1021/jacs.6b11148
J. Am. Chem. Soc. 2017, 139, 3417−3429

(23) Li, H. J.; Lai, C. T.; Pan, P.; Yu, W.; Liu, N.; Bommineni, G. R.; Garcia-Diaz, M.; Simmerling, C.; Tonge, P. J. *ACS Chem. Biol.* **2014**, *9*, 986−93.
(24) Lai, C. T.; Li, H. J.; Yu, W.; Shah, S.; Bommineni, G. R.; Perrone, V.; Garcia-Diaz, M.; Tonge, P. J.; Simmerling, C. *Biochemistry* **2015**, *54*, 4683−91.
(25) Wang, X.; Huang, B.; Liu, X.; Zhan, P. *Drug Discovery Today* **2016**, *21*, 118−32.
(26) Agalave, S. G.; Maujan, S. R.; Pore, V. S. *Chem. - Asian J.* **2011**, *6*, 2696−718.
(27) Theeramunkong, S.; Galli, U.; Grolla, A. A.; Caldarelli, A.; Travelli, C.; Massarotti, A.; Troiani, M. P.; Alisi, M. A.; Orsomando, G.; Genazzani, A. A.; Tron, G. C. *MedChemComm* **2015**, *6*, 1891−1897.
(28) Yu, W.; Neckles, C.; Chang, A.; Bommineni, G. R.; Spagnuolo, L.; Zhang, Z.; Liu, N.; Lai, C.; Truglio, J.; Tonge, P. J. *Anal. Biochem.* **2015**, *474*, 40−9.
(29) Rozwarski, D. A.; Vilcheze, C.; Sugantino, M.; Bittman, R.; Sacchettini, J. C. *J. Biol. Chem.* **1999**, *274*, 15582−9.
(30) Moree, B.; Yin, G.; Lazaro, D. F.; Munari, F.; Strohaker, T.; Giller, K.; Becker, S.; Outeiro, T. F.; Zweckstetter, M.; Salafsky, J. *J. Biol. Chem.* **2015**, *290*, 27582−93.
(31) Moree, B.; Connell, K.; Mortensen, R. B.; Liu, C. T.; Benkovic, S. J.; Salafsky, J. *Biophys. J.* **2015**, *109*, 806−15.
(32) Salafsky, J. S. *J. Chem. Phys.* **2006**, *125*, 074701.
(33) Salafsky, J. S.; Cohen, B. *J. Phys. Chem. B* **2008**, *112*, 15103−7.
(34) Salafsky, J. S. *Phys. Chem. Chem. Phys.* **2007**, *9*, 5704−11.
(35) Tian, G.; Paschetto, K. A.; Gharahdaghi, F.; Gordon, E.; Wilkins, D. E.; Luo, X.; Scott, C. W. *Biochemistry* **2011**, *50*, 6867−78.
(36) Schoop, A.; Dey, F. *Drug Discovery Today: Technol.* **2015**, *17*, 9−15.
(37) Massarotti, A.; Aprile, S.; Mercalli, V.; Del Grosso, E.; Grosa, G.; Sorba, G.; Tron, G. C. *ChemMedChem* **2014**, *9*, 2497−508.
(38) Totobenazara, J.; Burke, A. J. *Tetrahedron Lett.* **2015**, *56*, 2853−2859.
(39) Gerusz, V.; Denis, A.; Faivre, F.; Bonvin, Y.; Oxoby, M.; Briet, S.; LeFralliec, G.; Oliveira, C.; Desroy, N.; Raymond, C.; Peltier, L.; Moreau, F.; Escaich, S.; Vongsouthi, V.; Floquet, S.; Drocourt, E.; Walton, A.; Prouvensier, L.; Saccomani, M.; Durant, L.; Genevard, J. M.; Sam-Sambo, V.; Soulama-Mouze, C. *J. Med. Chem.* **2012**, *55*, 9914−28.
(40) Parikh, S. L.; Xiao, G.; Tonge, P. J. *Biochemistry* **2000**, *39*, 7645−50.
(41) Copeland, R. A. *Methods Biochem. Anal.* **2005**, *46*, 1−265.
(42) Collins, L.; Franzblau, S. G. *Antimicrob. Agents Chemother.* **1997**, *41*, 1004−9.

DOI: 10.1021/jacs.6b11148
J. Am. Chem. Soc. 2017, 139, 3417−3429